

# Advanced High-Power-Density Interior Permanent Magnet Motor for Traction Applications

Ayman M. EL-Refaie, *Fellow, IEEE*, James P. Alexander, Steven Galioto, Patel B. Reddy, *Member, IEEE*, Kum-Kang Huh, *Member, IEEE*, Peter de Bock, and Xiochun Shen

**Abstract**—Electric drive systems, which include electric machines and power electronics, are a key enabling technology for advanced vehicle propulsion systems that reduce the petroleum dependence of the ground transportation sector. To have significant effect, electric drive technologies must be economical in terms of cost, weight, and size while meeting performance and reliability expectations. This paper will provide details of the design, analysis, and testing of an advanced interior permanent magnet (PM) machine that was developed to meet the FreedomCAR 2020 specifications. The 12-slot/10-pole machine has segmented stator structure equipped with fractional-slot nonoverlapping concentrated windings. The rotor has a novel spoke structure/assembly. Several prototypes with different thermal management schemes have been built and tested. This paper will cover the test results for all these prototypes and highlight the tradeoffs between the various schemes. Due to the high machine frequency ( $\sim 1.2$  kHz at the top speed), detailed analysis of various loss components and ways to reduce them will be presented. In addition, due to the high coolant inlet temperature and the fact that the machine is designed to continuously operate at  $180^{\circ}\text{C}$ , detailed PM demagnetization analysis will be presented. The key novelty in this paper is the advanced rotor structure and the thermal management schemes.

**Index Terms**—Concentrated windings, fractional slot, interior, machine, permanent magnet (PM), synchronous, traction.

## I. INTRODUCTION

THE objective of this work is to develop high-power-density high-efficiency permanent magnet (PM) motors at a lower cost. The FreedomCAR 2020 required motor set of specifications is summarized in Table I and Fig. 1 [1]. It can be seen that this is a very challenging set of specifications, which includes the following: maximum speed of 14 000 r/min,

TABLE I  
FREEDOMCAR 2020 ADVANCED MOTOR PERFORMANCE REQUIREMENTS

Requirement	Target	Condition
Minimum top speed	14,000 rpm	
Peak output power	55 kW for 18sec	at 20% speed and nominal voltage
Continuous output power	30 kW	at 20~100% speed and nominal voltage
Weight	$\leq 35$ kg	
Volume	$\leq 9.7$ L	
Unit cost	$\leq \$275$	in quantities of 100,000
Operating DC bus voltage	200~450V, 325V nominal	
Maximum phase current	400Arms	
Characteristic current	$<$ Max. current	
Efficiency	$> 95\%$	at 10~100% speed for 20% rated torque
Line-to-line Back-EMF	$< 600$ V peak	at 100% speed
Torque pulsation	$< 5\%$ peak torque	at any speed
Ambient operating temp.	-40~140°C	outside housing
Coolant inlet temperature	105°C	
Max. coolant flow rate	10 liters/min	
Max. coolant pressure drop	2 psi	
Max. coolant inlet pressure	20 psi	
Min. isolation impedance	1MΩ	terminals to ground

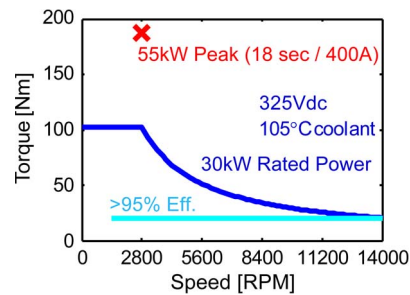


Fig. 1. FreedomCAR 2020 motor specified torque–speed curve.

Manuscript received July 1, 2013; revised November 7, 2013 and February 4, 2014; accepted February 7, 2014. Date of publication February 12, 2014; date of current version September 16, 2014. Paper 2013-EMC-561.R2, presented at the 2013 IEEE Energy Conversion Congress and Exposition, Denver, CO, USA, September 16–20, and approved for publication in the IEEE TRANSACTIONS ON INDUSTRY APPLICATIONS by the Electric Machines Committee of the IEEE Industry Applications Society.

A. M. EL-Refaie, J. P. Alexander, S. Galioto, P. B. Reddy, and K.-K. Huh are with the Electrical Machines Laboratory, GE Global Research Center, Niskayuna, NY 12309 USA (e-mail: elrefaie@research.ge.com; alexandj@ge.com; galioto@ge.com; reddy@ge.com; hukh@research.ge.com).

P. de Bock and X. Shen are with the Thermal Systems Laboratory, GE Global Research Center, Niskayuna, NY 12309 USA (e-mail: debock@research.ge.com; xiaochun.shen@gmail.com).

Color versions of one or more of the figures in this paper are available online at <http://ieeexplore.ieee.org>.

Digital Object Identifier 10.1109/TIA.2014.2305804

continuous power of 30 kW over 20%–100% speed range, peak power of 55 kW for 18 s at 20% speed, minimum efficiency of 95% over 10%–100% speed range, 105 °C cooling inlet temperature, fixed nominal 325-V dc source, approximately twice the power densities (at maximum speed) of the present state of the art [2], and an aggressive cost target of per unit for mass manufacturing in quantities of 100 000 s.<sup>1</sup>

<sup>1</sup>The material is based upon work supported by the DOE under award number DE-FC26-07NT43122.

Using segmented stator structures equipped with fractional-slot nonoverlapping concentrated windings (FSCW) have numerous well-established advantages associated with this type of windings, including high slot fill factor, short end turns, and high efficiency and power density [3]. In addition, they reduce cogging torque [4]. Recently, it has been shown that the conditions for optimal flux weakening can be achieved in a surface PM (SPM) by using FSCW [5], [6]. It has been also shown that using FSCW along with a higher number of phases helps make an SPM machine fault tolerant [7].

One of the key challenges with these winding configurations is the high eddy-current loss generated in the rotor mainly due to the presence of subharmonics as the synchronous MMF component is generally of a higher space harmonic order than unity [3], [6]. Various loss components in FSCW PM machines have been addressed in literature. Both circumferential and axial segmentations of the magnets have been proposed [8], [9]. The effect of the number of phases on the rotor losses has been also investigated [10]. The effect of axial segmentation and copper cladding on retaining sleeve losses for high-speed applications, too, has been investigated [11]. The losses in the stator support structure have been investigated in [12]. The losses in the rotor support structure have been investigated in [13]. In general, there is good understanding of the various loss components and how to mitigate them.

In [14], the performance of a conventional interior PM (IPM) design and a conventional SPM design, both of which are equipped with FSCW and segmented stator structures and targeting the Department of Energy (DOE) 2020 specifications, has been presented. This paper showed the benefits of segmented stator structures and FSCW. In this paper, the design, analysis, and test results of an advanced IPM design with a novel rotor structure and a segmented stator structure equipped with FSCW will be presented. This design has significant improvement in torque density ( $\sim 25\%$ ) compared with the designs presented in [14] and comparable or better efficiencies depending on the region of operation.

The key tradeoff in terms of an IPM rotor structure is the sizing of the bridges and center posts. On one hand, thick bridges and center posts are needed to withstand the high mechanical stresses at the maximum speed (14 000 r/min). On the other hand, thin bridges and center posts are needed to minimize the shunting of the PM flux in these regions [15]–[17]. This paper presents a novel spoke rotor structure/assembly that addresses this tradeoff.

The design and analysis details will be addressed in Section II. The prototypes construction will be addressed in Section III. The test results will be addressed in Section IV. A comparison of the various thermal management schemes will be presented in Section V, followed by conclusions in Section VI.

## II. MACHINE DESIGN AND ANALYSIS

After performing a tradeoff study between various IPM rotors and winding configurations, a 10-pole/12-slot IPM machine using high-strength sintered NdFeB magnets with 12 individually wound tooth structures, making it a double-layer

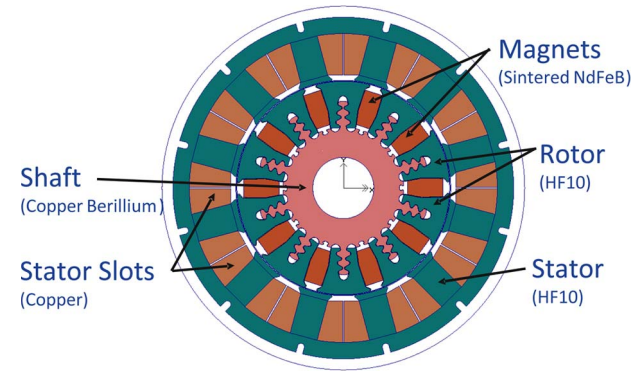


Fig. 2. Cross section of the full motor.

TABLE II  
KEY MACHINE DIMENSIONS

Stator outer diameter	280 [mm] including housing
Rotor outer diameter	142 [mm]
Airgap thickness	0.73 [mm]
Stack length	80 [mm]

TABLE III  
SUMMARY OF MOTOR MATERIALS

Stator/Rotor Laminations	DI-MAX HF-10 by AK Steel (10 mils or 0.25 mm thickness) $\sim [1\$/lb]$
Stator Cooling Tubes	Non-magnetic Stainless Steel 300 series $\sim [2\$/lb]$
Permanent magnets	VACODYM 890 TP $\sim [50\$/lb]$
Rotor wedges	Non-metallic composite that has temperature rating up to 240 °C $\sim [75\$/lb]$
Rotor shaft	Copper beryllium alloy (extrudable and has high thermal conductivity) $\sim [4\$/lb]$

winding pattern, was down-selected based on the highest torque density and efficiency. The machine has a novel spoke rotor structure/assembly, as shown in the machine cross section in Fig. 2. The rotor laminations are dovetailed into the nonmagnetic shaft. The PMs are wedged in between the rotor poles with nonmagnetic wedges at the top and bottom. This novel rotor structure/assembly eliminates the need for bridges and center posts while being able to sustain the mechanical stresses at higher speeds (conventional spoke rotors have bridges and have mechanical challenges in terms of going to high speeds). This configuration also provides flux-concentration effect (which is an inherent feature of a spoke design). Both of these aspects have significant impact on improving the torque/power density of the machine compared with v-shaped IPM designs. The key machine dimensions are summarized in Table II, whereas the materials used are summarized in Table III. Some approximate values for the materials' prices are also included. It has to be kept in mind that these prices will vary based on mass production. In addition, in some of the expensive materials such as the rotor wedges, a very small quantity is used.

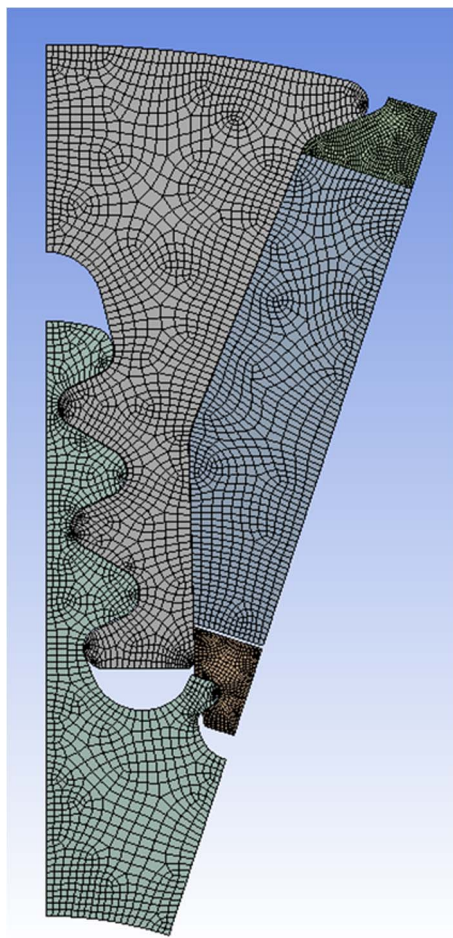


Fig. 3. Mesh used for stress analysis.

Here, a sample of the various type of analyses performed on the machine will be presented. More complete results will be included in conjunction with the test results in Section IV.

#### A. Mechanical Analysis

One of the key and most critical aspects of any design, particularly one that goes to a high speed of 14 000, with a novel rotor structure is the mechanical analysis. We need to make sure of the rotor structural integrity, particularly at the top speed. A detailed mechanical analysis, including stress, rotor dynamics, and life analyses, has been performed. Fig. 3 shows the mesh used for the mechanical analysis. Figs. 4–7 show the stress distribution in the rotor lamination, rotor shaft, bottom wedge, and top wedge, respectively, at 14 000 r/min. It can be seen that the stresses in all these components do not exceed the mechanical strength of the materials used and summarized in Table IV.

Fig. 8 shows a sample of the rotor dynamics analysis results. The figure shows that the first critical speed occurs at 24 000 r/min, which is much higher than the 14 000-r/min top speed of the machine.

To ensure that the design meets the life requirements, Fig. 9 shows that the design lies within the infinite life region of the Goodman diagram.

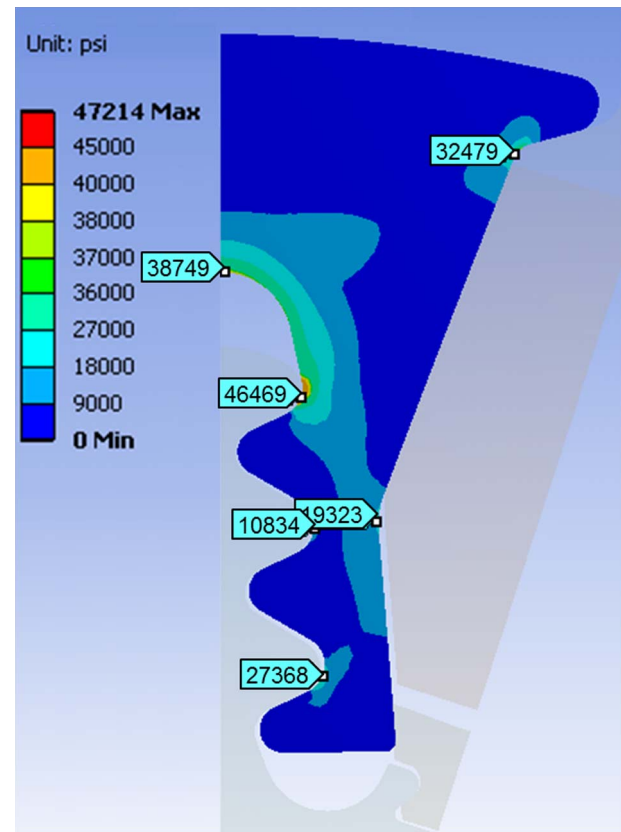


Fig. 4. Stress distribution in the rotor lamination at 14 000 r/min.

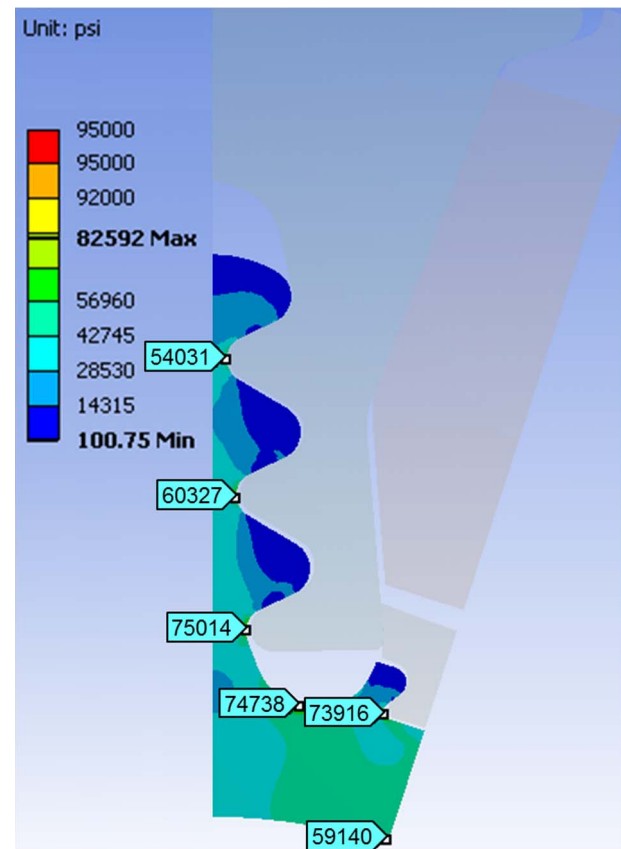


Fig. 5. Stress distribution in the rotor shaft at 14 000 r/min.

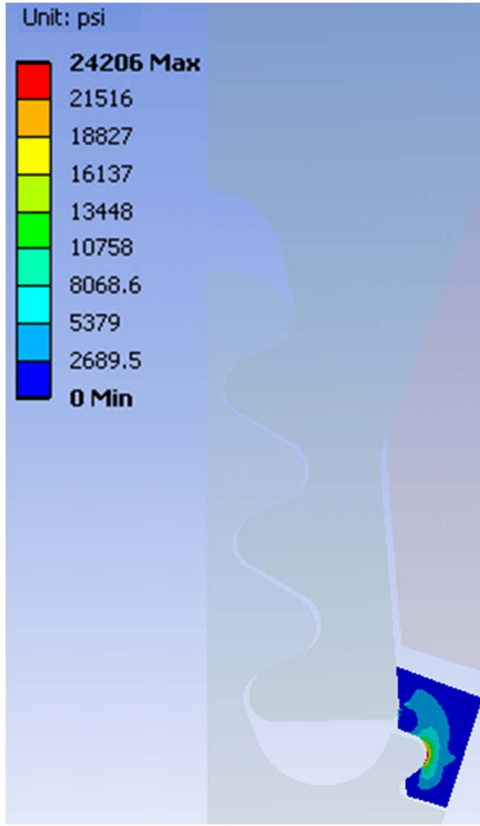


Fig. 6. Stress distribution in the rotor bottom wedge at 14 000 r/min.

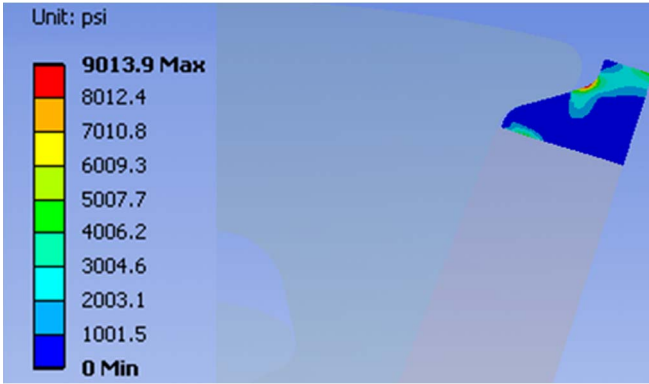


Fig. 7. Stress distribution in the rotor top wedge at 14 000 r/min.

TABLE IV  
MAXIMUM ALLOWABLE STRESS LIMIT FOR ROTOR COMPONENTS

Component	Stress Limit [ksi]	Stress Limit [MPa]
Rotor laminations	50	345
Rotor shaft	85	586
Rotor wedges	20	138

### B. Electromagnetic Analysis

The machine various performance aspects have been fully evaluated using finite element analysis (FEA). A sample of the key results will be covered here.

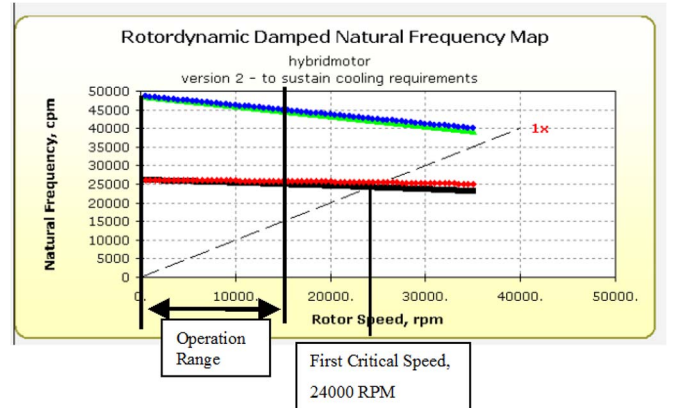


Fig. 8. Sample of the rotor dynamics analysis.

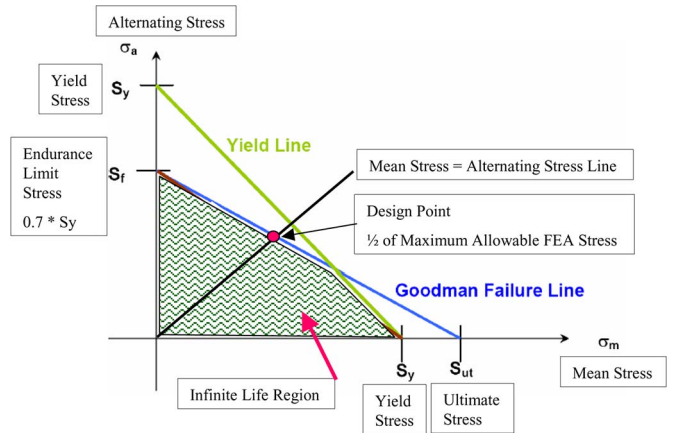


Fig. 9. Location of the design within the Goodman diagram.

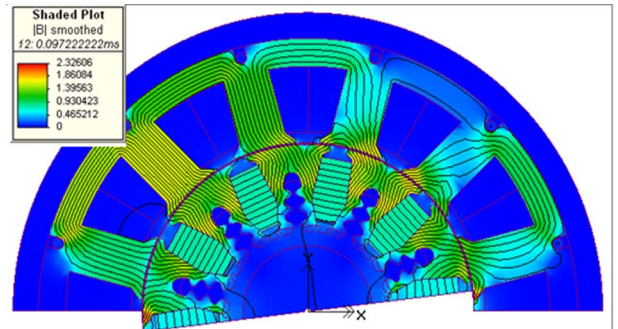


Fig. 10. Flux pattern for a 12 000-r/min open-circuit transient simulation.

1) *Open Circuit Results:* The machine open circuit performance has been checked using transient FEA with motion. Fig. 10 shows a snapshot of the open circuit flux pattern at 12 000 r/min. The key observation is that there is minimum/no magnet flux leakage due to the elimination of the bridges in this novel rotor structure. The machine back electromotive force (EMF) waveforms at 14 000 r/min are shown in Fig. 11.

2) *Demagnetization and SC Results:* It is well known that PMs become more prone to demagnetization at elevated temperatures. In addition, in applications where a wide constant power speed range (CPSR) is required, as in the case of this machine (CPSR of 5:1), the machine operates deep into flux weakening, and most of the current is along the negative

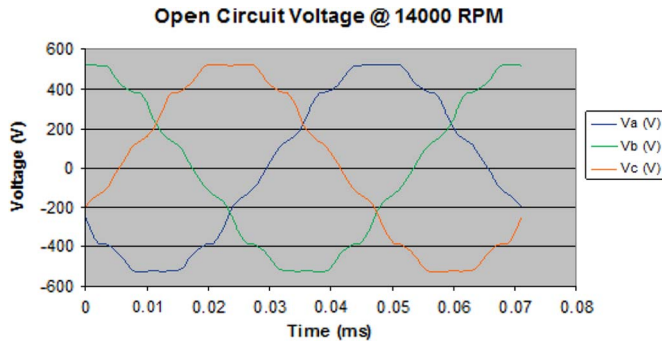


Fig. 11. Back EMF waveforms at 14 000 r/min.

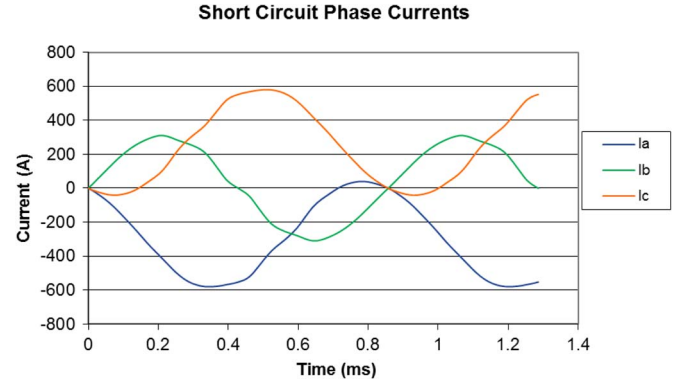


Fig. 13. Three-phase SC currents.

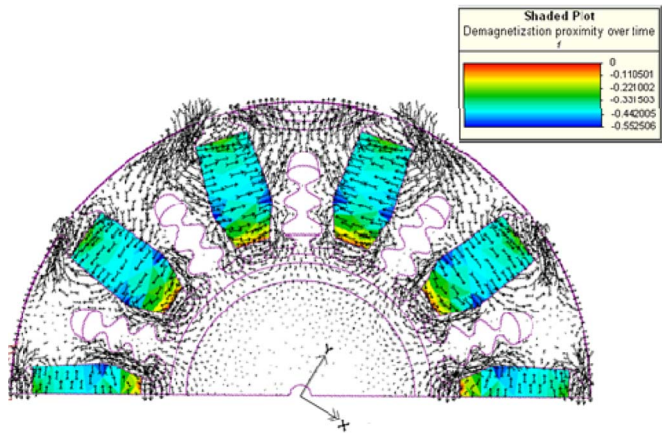


Fig. 12. Demagnetization at 2× rated current [320 Arms].

*d*-axis. In this case, the magnets are also more prone to demagnetization.

In the case of the machine under consideration, it is designed to continuously operate at 180 °C. At such high temperature, it is important to check that the magnets are safe in terms of demagnetization. It is also important to check this at both the highest operating temperature and under fault condition(s), during which the negative  $I_d$  current component can transiently be several times higher compared with the machine rated current.

Magnets demagnetization has been evaluated at 2× (see Fig. 12), 3×, and 4× the machine rated current injected along the negative *d*-axis and at 180 °C. Fig. 12 shows a shaded plot of the proximity of the B inside the magnets to a certain threshold ("0" value is used for this analysis, although the actual demagnetization knee of the magnet B–H curve is in the third quadrant). Demagnetization proximity values above zero indicate a flux density vector that is in opposition to the magnetization direction of the magnet. The shaded plot uses a composite of the flux densities within the magnets at every time instant within a full electrical cycle to determine the worst case for demagnetization. The flux density required for demagnetization at 150 °C is  $-0.55$  T or a demagnetization proximity value of  $+0.55$  T. Fig. 12 also includes arrow plots. If there is a direction reversal in the magnets, this is an indication of demagnetization. It can be seen that at 2× the machine rated current, there are no signs of demagnetization. At 3× the machine rated current, there is some local demagnetization (positive values and direction reversal) mainly at the bottom

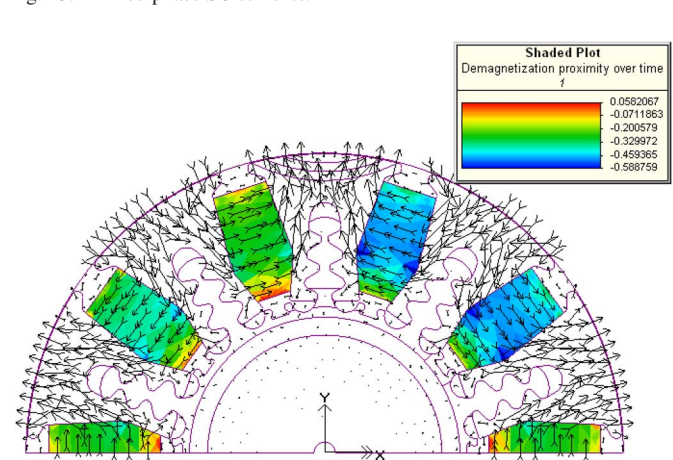


Fig. 14. Demagnetization under three-phase SC condition.

and slightly at the top of the magnets (not shown due to space limitation). At 4× the machine rated current, there are signs of more demagnetization (higher positive values) in the same locations. It is expected that the maximum transient current under symmetrical three-phase short-circuit (SC) condition should be around 2–3× the machine rated current; thus, there should be no demagnetization issues. In order to confirm these results, demagnetization has been evaluated under symmetrical three-phase SC condition. The focus has been on the initial transient SC current and its effect on the magnets. The resulting currents are shown in Fig. 13. The peak transient current is  $\sim 600$  A, which is  $\sim 2.65$ × the machine rated current. The demagnetization results are shown in Fig. 14. It can be seen that there are no signs of demagnetization indicated by a maximum demagnetization proximity value less than 0.55 T.

3) *Loss Calculations*: As previously mentioned, due to the high frequency of the machine ( $\sim 1.2$  kHz at 14 000 r/min), the high operating temperature of 180 °C, and the additional harmonic components introduced due to the use of FSCW, it is very critical to evaluate the various loss components and minimize them as much as possible. This section will cover the calculation of the various loss components on both the stator and rotor sides. Although the main focus will be on the traditionally more dominant loss components, including copper losses, core losses, and magnet losses, the section will cover other loss components that need to be checked to make sure that they are within acceptable thermal and efficiency limits.

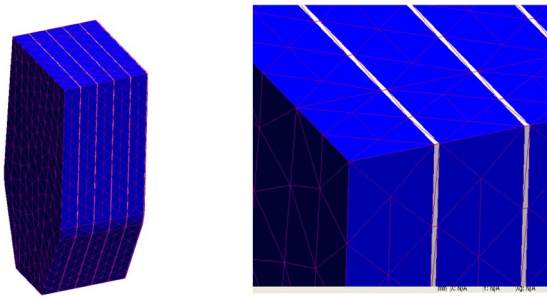


Fig. 15. Two-millimeter PM segments within a 3-D transient FE model.

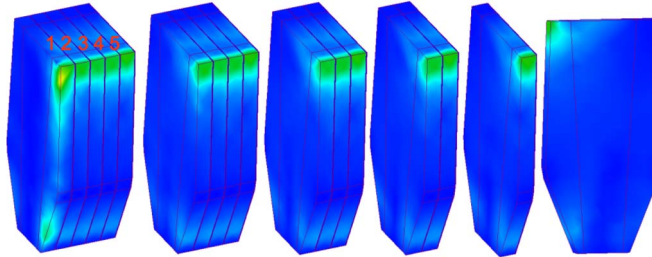


Fig. 16. Loss density shaded plot for 2-mm PM segments.

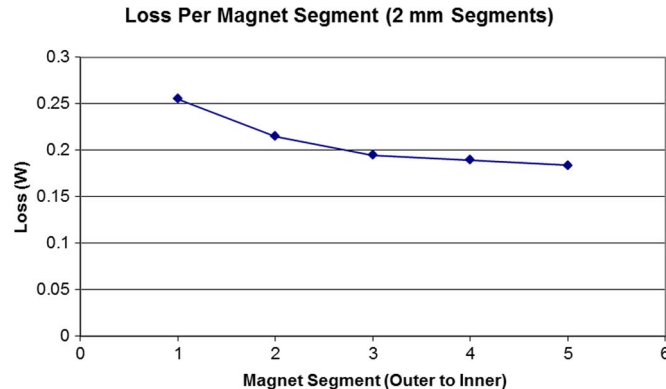


Fig. 17. Magnet loss per segment from the outermost segment to the innermost segment.

A 3-D finite element (FE) transient simulation of the motor is used to calculate PM losses; the model is shown in Fig. 15. In the actual motor, each pole of the motor contains a stack of “coffin-shaped” PMs, which stretch the entire length of the rotor core. The stack of magnets is composed of 2-mm axial segments of PM material with an insulating epoxy coating between adjacent segments. In the FE model, only five segments are modeled within a single pole, as shown in Fig. 16. Each segment is treated as a solid conducting region with a 0.1-mm insulating gap between adjacent magnet segments. The magnet segments are placed toward one axial end of the motor model in order to capture the fringing field effects toward the end of the motor. The outermost axial segment has the greatest loss density due to the fringing magnetic field it experiences toward the end of the motor. As shown in Fig. 17, the loss per magnet decreases from the outermost magnet to the innermost magnet. The loss in all of the PM material within the motor is calculated as 130 W at rated load and 14 000 r/min. This loss represents the greatest expected PM loss for all rated operating points.

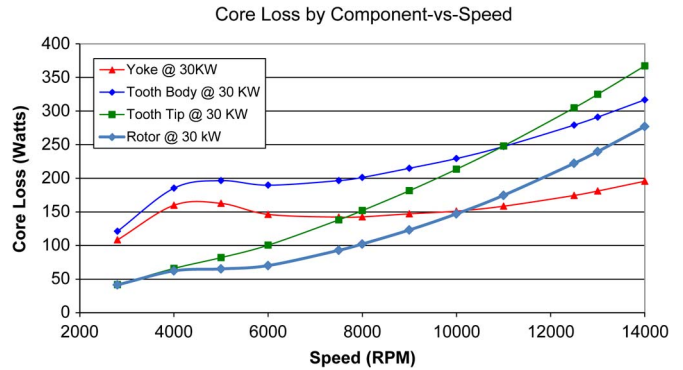


Fig. 18. Core loss versus speed under continuous power operating conditions.

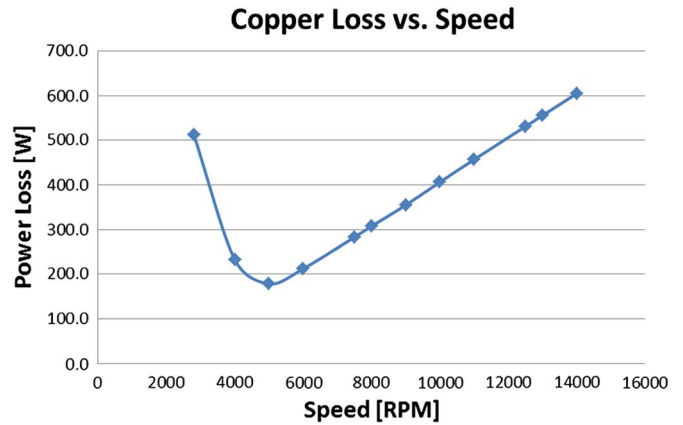


Fig. 19. Copper loss versus speed under continuous power operating conditions.

The most dominant loss component, which is the stator/rotor core losses, has been calculated on an element-by-element basis using 2-D FEA. The breakdown of the stator and rotor core losses under the continuous power conditions is given in Fig. 18. As expected, all components increase with speed/frequency, whereas the stator yoke losses are the least sensitive to variation of speed.

Another key loss component is copper losses. Fig. 19 shows copper losses under continuous power operating conditions as a function of speed. These losses are evaluated at 180 °C. In addition, ac losses (including skin and proximity effects) are taken into consideration. The winding strand size has been chosen such that the ac losses at 14 000 r/min (~1.2 kHz) contribute less than 10% additional losses.

It can be seen that the copper losses are the highest at the rated torque at 2800-r/min corner speed. As the torque starts dropping, the current and, hence, copper losses start dropping until the voltage limit is reached at around 5000 r/min. After that, the current and, hence, copper losses start increasing as a function of speed due to the increase in negative  $I_d$  component required for flux weakening.

It is important not to overlook any loss component even if the perception is that it might not be significant, particularly in the case of the machine design under consideration since it has an unconventional rotor arrangement where the shaft is an integral part of the magnetic circuit as well, having various components as a part of the thermal management scheme(s).

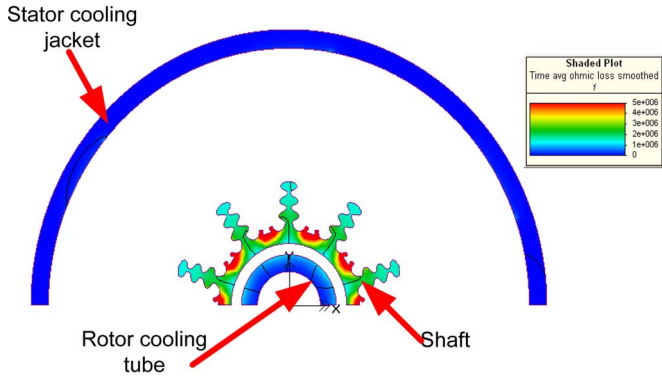


Fig. 20. Time-averaged ohmic loss density in solid conducting components at peak power and 2800 r/min.

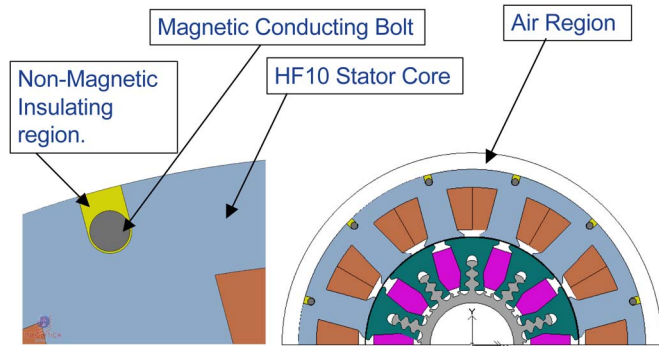


Fig. 21. FEA model of the motor with bolts in stator core.

Shaft, rotor cooling tube (as will be discussed in the thermal analysis section), and stator cooling jacket electrical losses are calculated using 2-D FE transient simulations with solid conducting components. Fig. 20 shows a shaded loss density plot for all three conducting components at peak power and 2800 r/min as an example. There is negligible loss in the cooling jacket located exterior to the stator yoke and in the cooling tube located interior to the rotor shaft. The spoke shaft has the greatest loss density. Careful optimization/shaping of the shaft reduced the eddy current losses to 880 W at 55 kW and 2800 r/min and 440 W at 30 kW and 14 000 r/min. The key optimization was related to the size and shape of the “notches” that can be seen near the shaft inner radius. These notches proved to be very effective in terms of reducing the shaft losses mainly due to the stator MMF fundamental subharmonic that penetrates deep into the rotor.

A 2-D transient simulation is used to quantify the electrical losses in the bolts that clamp the frame of the motor to its stator core structure. The bolts are modeled as solid magnetic conductors at the back of the stator core, as shown in Fig. 21. The actual motor as built contains stainless steel bolts; the electrical resistivity used in the model is the same as that of stainless steel. However, in order to be conservative, this analysis is run with a nonlinear magnetic B–H curve that is exactly the same as the HF10 stator core material. Small nonmagnetic regions are modeled as “insulating” regions around the individual bolts, as shown in Fig. 21. All of the bolts are connected in parallel and shorted at the ends. This assumes that the motor’s frame shorts the bolts on either end of the motor. Fig. 21 shows that almost no magnetic flux traverses across the bolts at the back of the

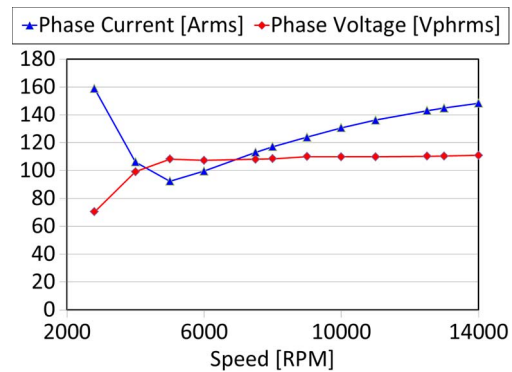


Fig. 22. Motor output current and voltage versus speed under continuous power conditions.

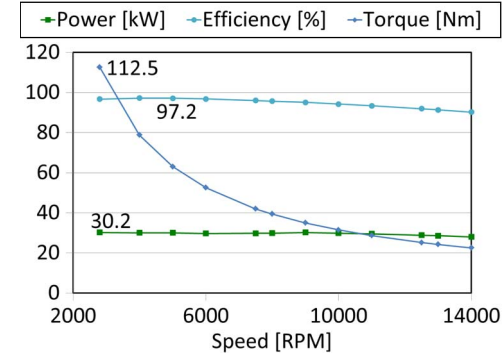


Fig. 23. Motor output power, torque, and efficiency versus speed under continuous power conditions.

stator core. The ohmic loss in the bolts for the entire motor is  $\sim 10$  W. It was critical in this case to prevent the stator flux from fully enclosing the bolts, and that is why, by design, the bolts fit in a “u-shaped” type of space with the bolts insulated to prevent the creation of a cage in order to minimize the losses. If this detail was not taken into consideration, the bolt losses can be significantly higher.

**4) Motor Performance Under Load:** The performance of the motor under continuous power conditions is shown in Figs. 22 and 23. It can be seen that the motor is capable of providing the required 30 kW over the entire speed range while staying within the current and voltage limits. The rated current is within 160 Arms, whereas the phase voltage is limited to 110 Vphrms. This voltage corresponds to a voltage of 175 VDC and is within the voltage specification of 200 VDC. The electromagnetic efficiency under the continuous power conditions is higher than 95% over a speed range of 11 000 r/min, whereas the top speed efficiency reached 92.7%. It has to be noticed that this efficiency does not include the mechanical losses. It is expected that the inclusion of mechanical losses will decrease the efficiency at higher speeds, as will be seen in the test results.

### C. Thermal Analysis

**1) Rotor Cooling:** Fig. 24 shows a schematic of the cooling scheme. The coolant available for the rotor is transmission oil at 105 °C inlet temperature. This coolant is introduced into the system via a coupling connected to a stationary inner

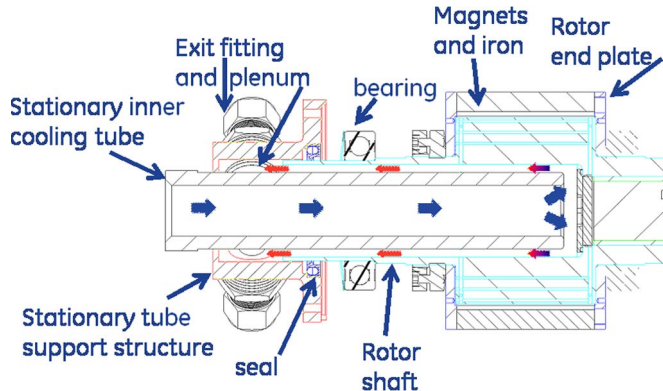


Fig. 24. Rotor cooling scheme.

cooling tube. The stationary tube sits inside the hollow rotor shaft and is supported by a structure that attaches it to the stator housing. The support is on one side of the tube. The part of the tube largely inside the rotor shaft is cantilevered. The cooling fluid flows inside the inner diameter (ID) of the stationary tube until it passes all the way through. It then enters a plenum area between the stationary tube and the shaft. At this location, the fluid travels radially outward to enter an annulus between the outer diameter (OD) of the stationary tube and the ID of the hollow shaft. The fluid experiences both axial flow and circumferential flow within this annulus. The axial flow is induced from the pressure difference between the entrance and the exit of the annulus space. It is provided by an external pump (not shown). The stationary tube OD as well as the rotor core ID have been optimized to maximize heat transfer coefficient and minimize the pressure drop. The inner bore heat transfer coefficient achieved ranged from  $800 \text{ W/m}^2 \cdot \text{K}$  (at 2800 r/min) to  $2900 \text{ W/m}^2 \cdot \text{K}$  (at 14000 r/min). Due to this cooling scheme, the choice of the copper beryllium shaft was important due to its mechanical strength and high thermal conductivity.

In order to increase the accuracy of the analysis, the rotor lamination, magnet, and shaft have been divided into several zones/segments, as shown in Fig. 25, and the losses in each of these zones are evaluated and used as inputs to the thermal model. The loss density in these zones as a function of speed under rated power operating conditions is shown in Fig. 26. Forced convection is assumed at the shaft ID, and the heat transfer coefficient assumed is dependent on speed, as previously mentioned. Fig. 27 shows the FEA results at 30 kW and 14 000 r/min. It can be seen that the maximum temperature is about  $180^\circ\text{C}$ , which is the design temperature and well within the thermal limits of the various rotor materials. The maximum rotor temperatures at various speeds and loading conditions are summarized in Fig. 28.

*2) Stator Cooling:* Three different stator cooling schemes have been evaluated, and three prototypes have been built and tested, as will be discussed later. All three prototypes have a cooling jacket shrunk fit at the stator OD with circumferential cooling passages, as shown in Fig. 29. The cooling channel diameter is 3.175 mm. The number of cooling channels, their shape, locations, and number of parallel paths were optimized to balance the achieved heat transfer coefficient versus pressure drop. The pressure drop is around  $2\text{--}3 \text{ lbf/in}^2$ , and the corresponding heat transfer coefficient is around  $1000 \text{ W/m}^2 \cdot \text{K}$ .

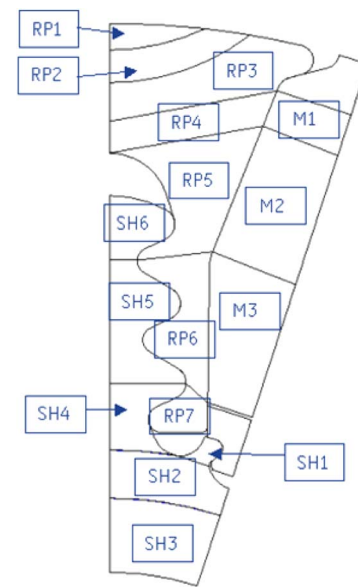


Fig. 25. Thermal model divided into zones.

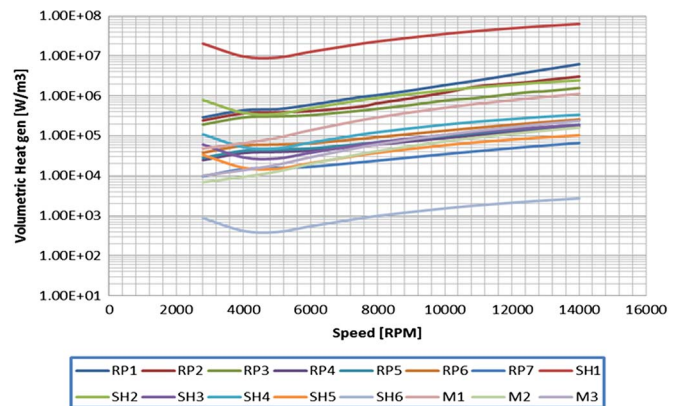


Fig. 26. Loss density in the various zones as a function of speed under rated power operating condition.

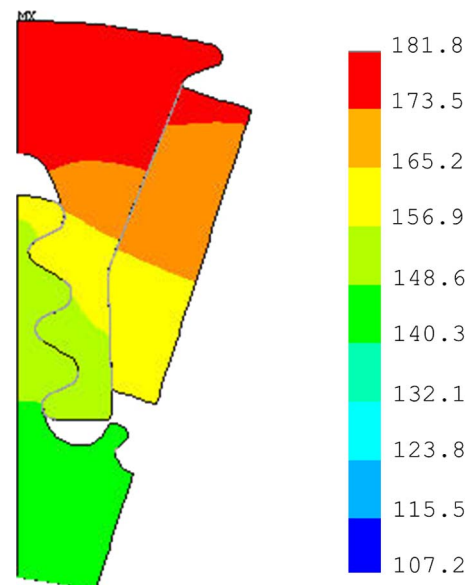


Fig. 27. Temperature distribution (in degrees celsius) of the rotor segment under worst case load at 30 kW and 14 000 r/min.

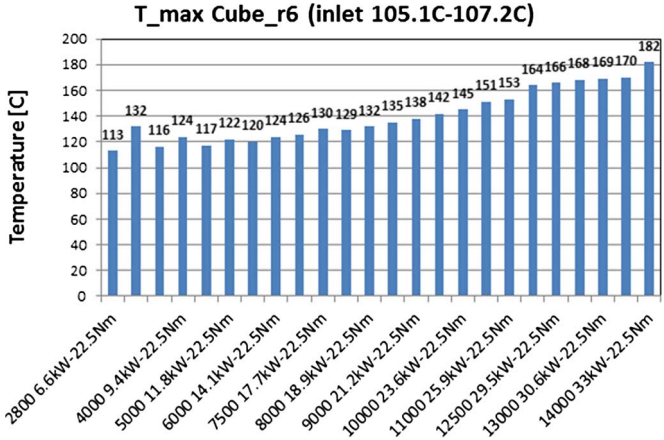


Fig. 28. Maximum rotor temperatures for all operating points.

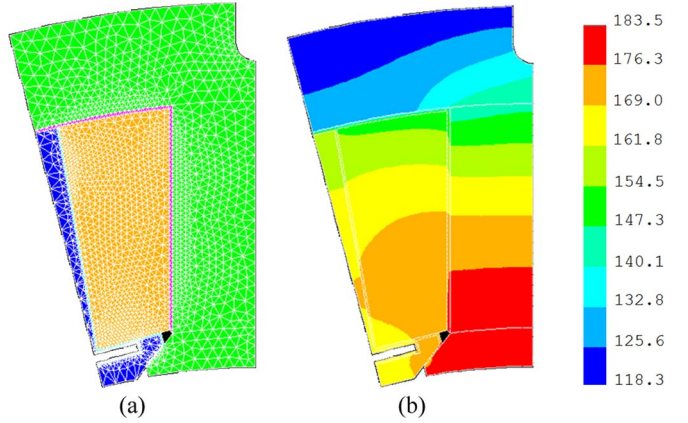


Fig. 32. Second prototype thermal FEA model and results at 30 kW and 14 000 r/min.

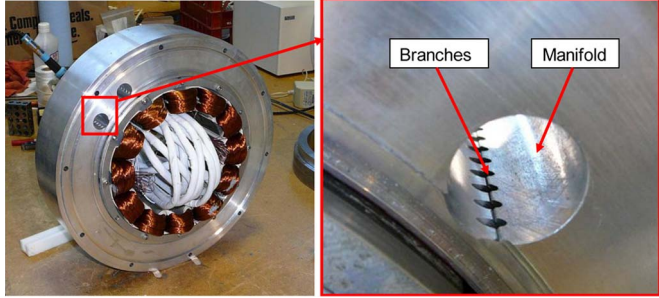


Fig. 29. Stator cooling jacket with microchannels.

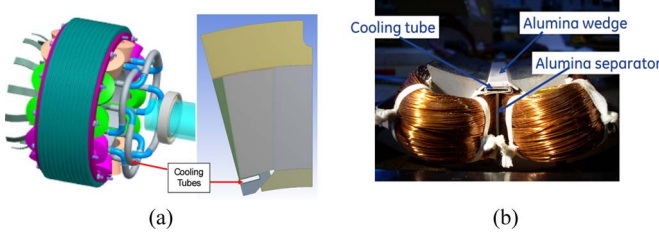


Fig. 30. Cooling tubes inside stator slots.

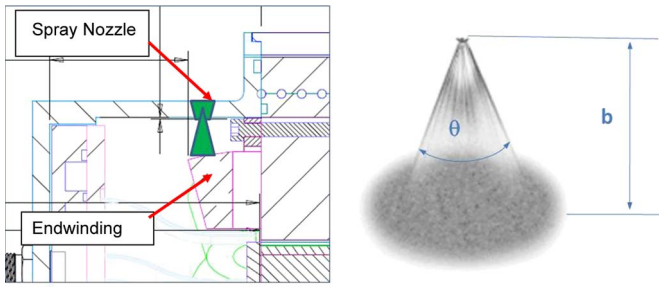


Fig. 31. End-winding spray cooling.

The second prototype has cooling tubes inside the stator slots, as shown in Fig. 30. The third prototype has nozzles for spray cooling the stator end windings, as shown in Fig. 31. Fig. 32 shows the FEA model for the second prototype (with cooling tubes in the stator slots) and the results at 30 kW and 14 000 r/min (most demanding thermal operating point). It can

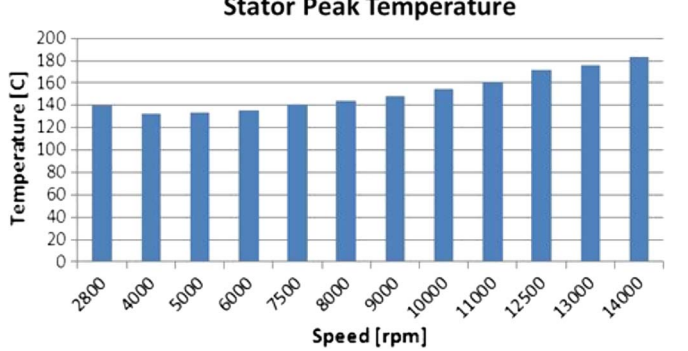


Fig. 33. Stator peak temperatures for the second prototype at 30 kW and different speeds.

be seen that the maximum stator temperature is around 180 °C. This is the hot spot temperature the machine was designed for, and it falls within the thermal limits of the class H insulation used. This model represents half of a stator slot and modeled the coil, insulation, lamination, and cooling tubes explicitly. The electric losses (copper and core) are modeled as heat source terms, and the convection boundary condition is applied on the stator OD and the cooling tubes. The hot spot in this case is in the stator tooth and not the in the middle of the coil because core losses are dominant at the top speed and due to the presence of the cooling tubes inside the stator slots, which provide direct cooling of the coils. Fig. 33 summarizes the stator peak temperatures for the same prototype at 30 kW and at various speeds.

### III. PROTOTYPE CONSTRUCTION

The 12-slot segmented stator structure along with a couple of teeth of the IPM machine is shown in Fig. 34. The novel 10-pole spoke rotor previously discussed is shown in Fig. 35, whereas the fully assembled motor is shown in Fig. 36. As can be seen, the rotor laminations are dovetailed into the nonmagnetic shaft. The PMs are wedged in between the rotor poles with nonmagnetic wedges at the top and bottom. All three prototypes using the three different cooling schemes previously discussed meet the 35-kg requirement. The thermal performance of the three prototypes is different, as will be discussed in Section V.

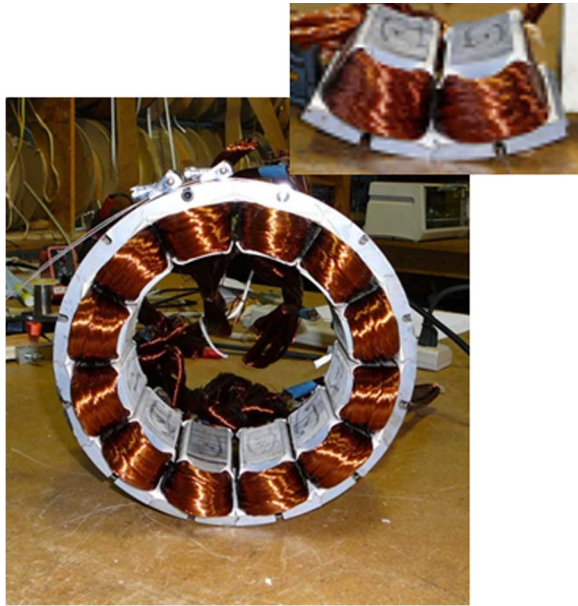


Fig. 34. Assembled 12-slot stator.

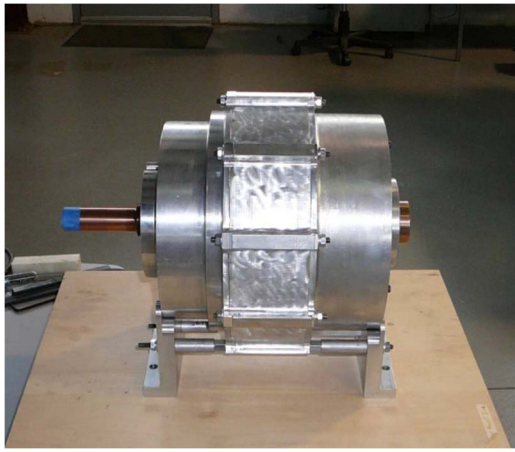


Fig. 35. Fully assembled motor.

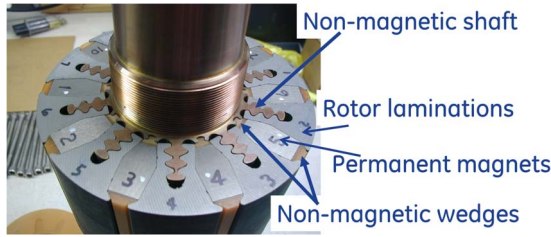


Fig. 36. Advanced PM spoke rotor.

#### IV. TEST RESULTS

This section will cover some of the test results of the second prototype with cooling tubes in the stator slots. Due to space limitations, full test results of all three prototypes cannot be included. The test setup is shown in Fig. 37. The test setup allows testing the machine at 105 °C coolant inlet temperature as required in the specifications. The following tests have been performed.

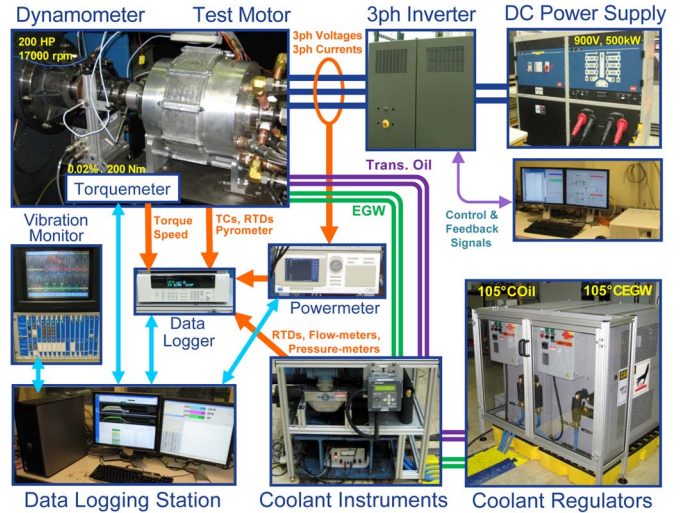


Fig. 37. Test setup.

TABLE V  
INSULATION TESTING

Insulation Test Method	Standard	Test Result
Insulation Resistance Polarization Index	IEEE 43	>100 GΩ 500V 1min >100 GΩ 500V 10min
AC HiPot	NEMA MG1 IEC 60034	1.6kV Pass

##### A. Insulation Testing

The insulation testing is done according to the standards summarized in Table V. HiPot testing is performed during and after assembly of the motor. Insulation resistance is regularly recorded during testing. Motor way exceeds the required 1-MΩ isolation phase impedance to ground.

##### B. Mechanical/Friction and Windage Losses Testing

The machine was first tested with unmagnetized magnets to separate mechanical losses (for the same rotor, the magnets were initially unmagnetized for the purpose of this test; then, they were magnetized and reinserted in the rotor for other tests). The test results are shown in Fig. 38. These losses include friction and windage, bearings, and seal losses. Based on the test results, more modifications were implemented to reduce mechanical losses at 14 000 r/min by ~35%, as shown in Fig. 38. This was achieved by reducing the rotor churning losses by optimizing the stationary tube OD and the rotor core ID and choosing different seals and bearings.

##### C. Back EMF (Open Circuit Voltage) Test

The machine was tested open circuit up to 14 000 r/min. The machine phase back EMF at 14 000 r/min was 388 Vrms.

##### D. Steady-State SC

The machine was tested under SC condition both using a short at the machine terminals and shorting the machine through the inverter. The RMS SC current is 183 Arms, which is close to the calculated machine characteristic current of 185 Arms.

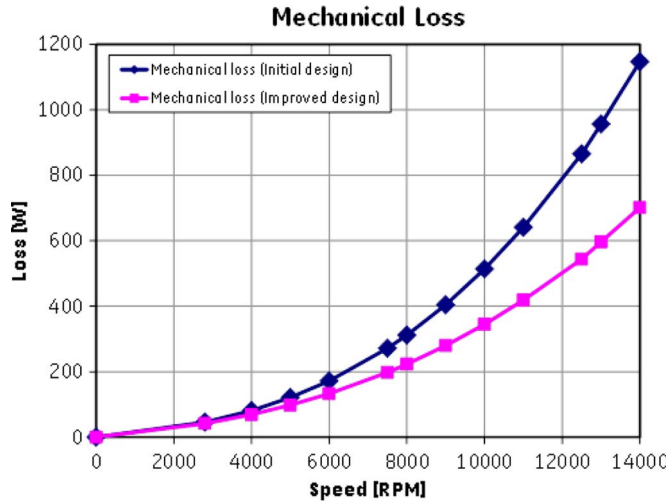


Fig. 38. Mechanical losses as a function of speed.

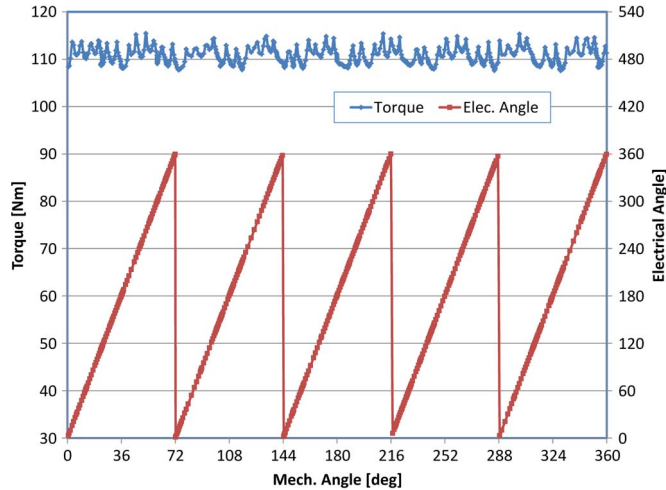


Fig. 39. Machine torque ripple.

### E. Torque Ripple

The machine torque ripple was tested under 1-r/min rated torque with 60 °C coolant soaked condition. The results are shown in Fig. 39. The maximum torque was 115.4 N · m, the minimum torque was 107.6 N · m, and the peak-to-peak ripple was 7.8 N · m. This corresponds to 4.2% peak-to-peak torque ripple versus peak torque < 5% specifications.

### F. Full Load Testing With a Converter

The machine was tested under various load conditions over the entire speed range using the power converter. First, the machine was tested under peak power (55 kW) condition at 2800 r/min. The test results are summarized in Fig. 40. Fig. 41 shows the temperature rises in various parts of the machine during the peak power testing. It can be seen that the maximum temperature rise is < 40 °C.

Fig. 42 shows the temperature rise in various parts of the machine during heat runs and rated power operating condition as a function of speed (in the case of cooling tubes in the stator slots). It can be seen that the maximum temperature rise in the machine is around 75 °C, which corresponds to 180 °C with 105 °C coolant inlet temperature. Temperatures in the stator

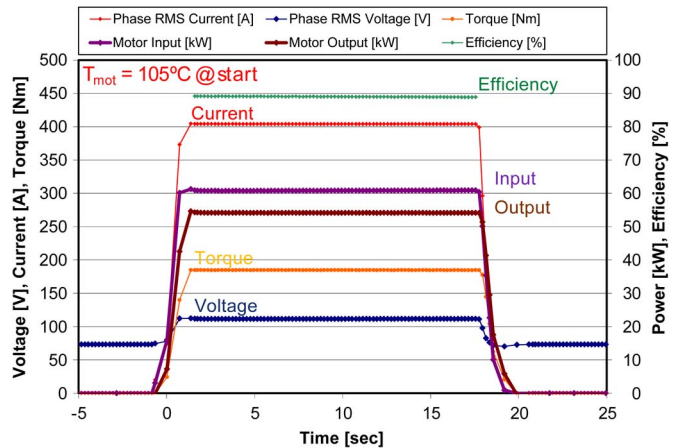


Fig. 40. Machine peak power testing at 2800 r/min for 20 s.

Peak Power applied for 20 sec at 2800 rpm with 95C coolant.

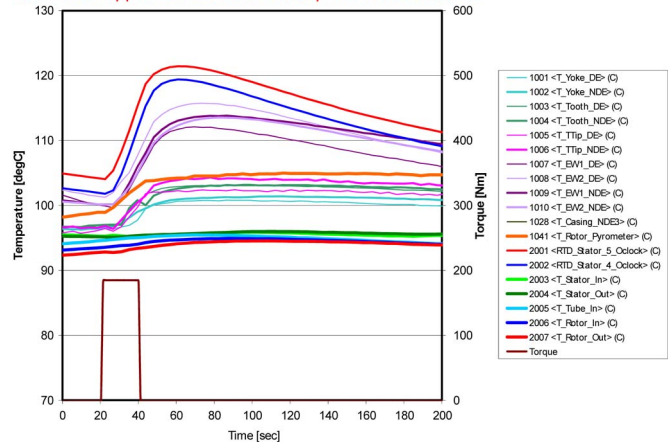


Fig. 41. Temperature rises inside the machine under peak power testing at 2800 r/min for 20 s.

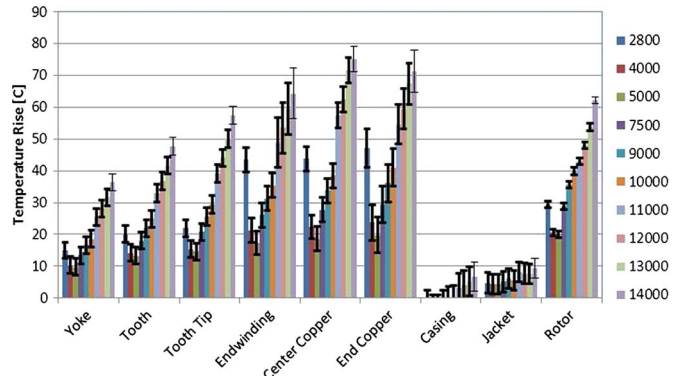


Fig. 42. Measured temperature rises inside the machine as a function of speed under rated power testing.

have been measured using thermocouples and resistance temperature detectors, as well as calorimetric measurements based on coolant flow rate and temperature rise. Rotor temperatures were measured using an infrared sensor (after painting one end of the rotor back and having windows in the rotor end plate to have access to the magnets) and calorimetric measurements.

Next, the machine was transiently tested at various load levels and speeds. The measured machine efficiency map is shown in Fig. 43. The machine efficiency is very advantageous compared with the state of the art, particularly at lower speeds

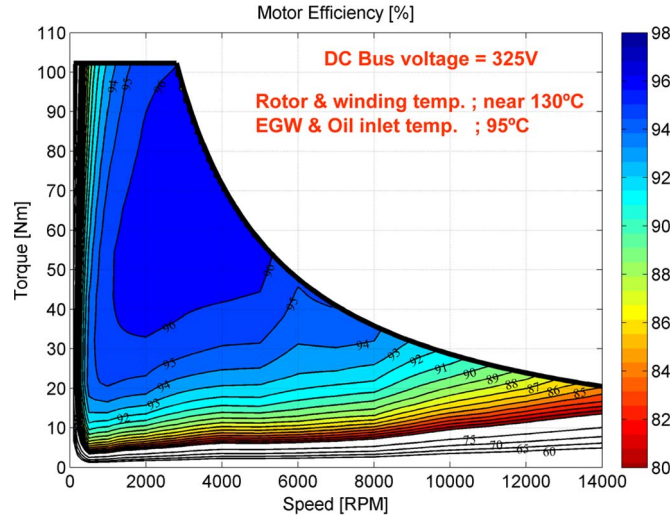


Fig. 43. Machine measured efficiency map.

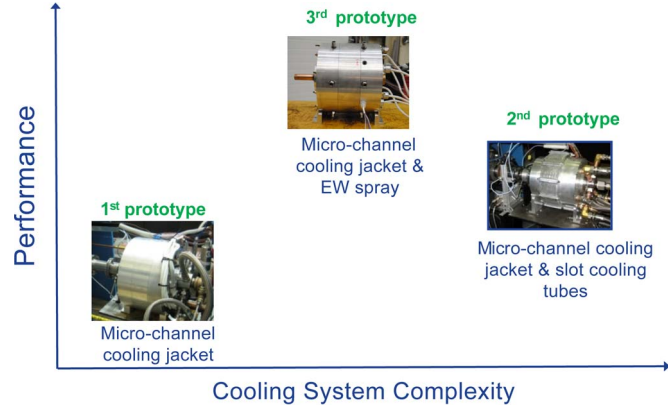


Fig. 44. Relative tradeoff between various cooling schemes.

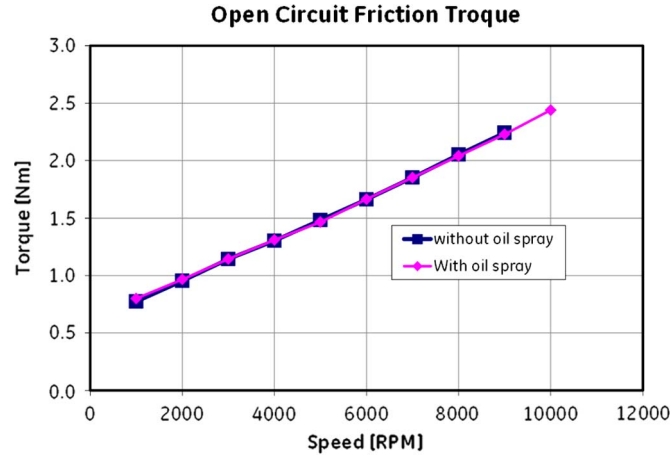


Fig. 45. Open circuit torque/losses with and without oil spray cooling.

[2]. In addition, it has to be kept in mind that this machine is designed for a lower nominal dc bus voltage of 325 V compared with the state of the art (650 V).

## V. VARIOUS COOLING SCHEMES

As previously discussed, three prototypes with different stator cooling schemes have been built and tested. The first two prototypes represent the baseline case. Fig. 44 shows how these

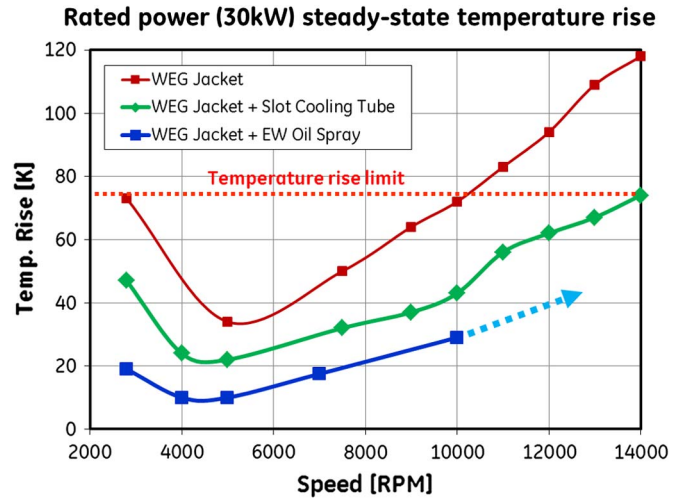


Fig. 46. Temperature rise along the 30-kW trajectory using the various cooling schemes.

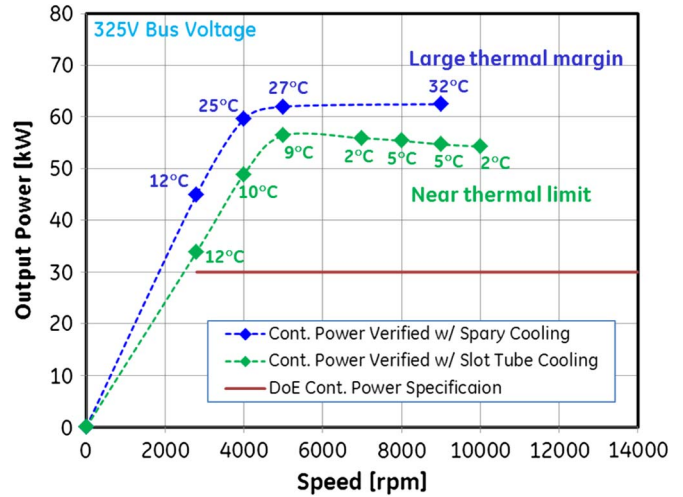


Fig. 47. Continuous power measured at various speeds with the thermal margin indicated at each operating point.

various cooling schemes compare in terms of performance and complexity. Fig. 45 shows the open circuit losses with and without oil spray cooling. It can be seen that the results are quite similar, indicating that the oil is successfully kept out of the air gap, which is a big risk, particularly at high speeds in terms of windage losses. This was achieved by having “oil deflectors” in the end region to minimize the risk of oil getting into the air gap. Fig. 46 shows the temperature rise along the 30-kW trajectory for all three schemes. The temperatures are measured in the middle of the stator coils. It can be seen that the spray cooling is the most effective and is fairly simple in terms of complexity. In addition, it is shown that the motor can be continuously run with 105 °C coolant over the entire speed range. The cooling jacket alone is not sufficient. The cooling tubes can meet the requirements but is more complicated and not very suitable for mass production. Fig. 47 shows the results for the heat runs performed to determine the maximum achievable continuous power out of the machine. As can be seen, the machine (in particular) with spray cooling is capable of more than 2× the required continuous power with a comfortable thermal margin. This gives room to extract more continuous power out of the

TABLE VI  
COMPARISON OF MACHINE PERFORMANCE (SECOND AND THIRD PROTOTYPES) VERSUS REQUIREMENTS

Items	Specification	Status and Result
<b>Max. Speed</b>	14,000rpm	Verified
<b>Peak Power</b>	55kW @ 20% speed for 18sec	Verified
<b>Maximum Current</b>	400Arms	Verified
<b>Cont. Power</b>	30kW @ 20~100% speed @ Vdc=325	Verified
<b>Efficiency</b>	>95% @ 10~100% speed @ 20% rated torque	> 94% @ 10~20% speed > 90% @ ~ 9000 rpm > 85% @ ~ 14000 rpm
<b>Operating Voltage</b>	200~450V (325V nominal)	Verified
<b>Back EMF</b>	<600Vpk line-to-line @ 100% speed	< 950Vpk line-to-line @ 14000 rpm
<b>Torque Pulsation</b>	<5% of Peak Torque @ any speed	4.2% of Peak Torque @ rated torque 1 rpm
<b>Characteristic Current</b>	< Maximum Current	185Arms
<b>Weight</b>	≤35kg	Verified
<b>Volume</b>	≤9.7L	Verified
<b>Cost @100k</b>	≤\$275	Not met
<b>Ambient (outside housing) Operating Temperature</b>	-40~140°C	Pending (expected not to be a challenge)
<b>Coolant inlet</b>	105°C, <10LPM, 2psi drop, <20psi inlet	Verified
<b>Minimum isolation impedance-phase terminal to GND</b>	1Mohm	>100Gohm @ 500V

machine. It is expected that the machine continuous power density (based on total mass) at 105 °C coolant inlet temperature will be around 2 kW/kg. This is a significant improvement compared with the state of the art [2].

## VI. CONCLUSION

This paper has presented the design, analysis, and test results for a novel high-power-density IPM motor for traction applications. The 12-slot/10-pole design has a segmented stator structure with FSCW and a novel spoke rotor structure that eliminates bridges. The details of the machine design and analysis have been presented. The prototype construction and the test results of one of the prototypes have been presented. Test results of three different cooling schemes have been presented and compared. Table VI summarizes the machine performance (of the second and third prototypes) versus requirements. It can be seen that this novel design can meet most of the very demanding FreedomCAR 2020 specifications, particularly in terms of power density and efficiency.

## REFERENCES

- [1] [Online]. Available: [www1.eere.energy.gov/vehiclesandfuels/about/partnerships/freedomcar/](http://www1.eere.energy.gov/vehiclesandfuels/about/partnerships/freedomcar/)
- [2] Evaluation of the 2007 Toyota Camry Hybrid Synergy Drive System. [Online]. Available: <http://www.osti.gov/bridge/servlets/purl/928684-rRNS3/928684.pdf>
- [3] A. M. El-Refaie, "Fractional-slot concentrated-windings synchronous permanent magnet machines: Opportunities and challenges," *IEEE Trans. Ind. Electron.*, vol. 57, no. 1, pp. 107–121, Jan. 2010.
- [4] J. Cros and P. Viarouge, "Synthesis of high performance PM motors with concentrated windings," *IEEE Trans. Energy Convers.*, vol. 17, no. 2, pp. 248–253, Jun. 2002.
- [5] A. M. EL-Refaie and T. M. Jahns, "Optimal flux weakening in surface PM machines using concentrated windings," *IEEE Trans. Ind. Appl.*, vol. 41, no. 3, pp. 790–800, May/Jun. 2005.
- [6] A. M. EL-Refaie, T. M. Jahns, P. J. McCleer, and J. W. McKeever, "Experimental verification of optimal flux weakening in surface PM machines using concentrated windings," *IEEE Trans. Ind. Appl.*, vol. 42, no. 2, pp. 443–453, Mar./Apr. 2006.
- [7] B. C. Mecrow, A. G. Jack, J. A. Haylock, and J. Coles, "Fault-tolerant permanent magnet machine drives," *Proc. Inst. Elect. Eng.—Electr. Power Appl.*, vol. 143, no. 6, pp. 437–442, Nov. 1996.
- [8] K. Atallah, D. Howe, P. H. Mellor, and D. A. Stone, "Rotor loss in permanent-magnet brushless ac machines," *IEEE Trans. Ind. Appl.*, vol. 36, no. 6, pp. 1612–1618, Nov./Dec. 2000.
- [9] J. D. Ede, K. Atallah, G. W. Jewell, J. B. Wang, and D. Howe, "Effect of axial segmentation of permanent magnets on rotor loss of modular brushless machines," in *Conf. Rec. IEEE IAS Annu. Meeting*, Oct. 2004, vol. 3, pp. 1703–1708.
- [10] A. M. El-Refaie, M. R. Shah, R. Qu, and J. Kern, "Effect of number of phases on conducting sleeve losses of high-speed surface PM machine rotors," *IEEE Trans. Ind. Appl.*, vol. 44, no. 5, pp. 1522–1530, Sep./Oct. 2008.
- [11] M. R. Shah and A. M. EL-Refaie, "Eddy current loss minimization in conducting sleeves of high speed machine rotors by optimal axial segmentation and copper cladding," *IEEE Trans. Ind. Appl.*, vol. 45, no. 2, pp. 720–728, Mar./Apr. 2009.
- [12] M. R. Shah and A. M. EL-Refaie, "End effects in multi-phase fractional-slot concentrated-winding surface permanent magnet synchronous machines," *IEEE Trans. Energy Convers.*, vol. 25, no. 4, pp. 1001–1009, Dec. 2010.

- [13] A. M. El-Refaie *et al.*, "Rotor end losses in multiphase fractional-slot concentrated-winding permanent magnet synchronous machines," *IEEE Trans. Ind. Appl.*, vol. 47, no. 5, pp. 2066–2074, Sep./Oct. 2011.
- [14] P. B. Reddy, A. M. EL-Refaie, K.-K. Huh, J. K. Tangudu, and T. M. Jahns, "Comparison of interior and surface PM machines equipped with fractional-slot concentrated windings for hybrid traction applications," *IEEE Trans. Energy Convers.*, vol. 27, no. 3, pp. 593–602, Sep. 2012.
- [15] E. C. Lovelace, T. M. Jahns, T. A. Keim, and J. H. Lang, "Mechanical design considerations for conventionally laminated, high-speed, interior PM synchronous machine rotors," *IEEE Trans. Ind. Appl.*, vol. 40, no. 3, pp. 806–812, May/Jun. 2004.
- [16] A. M. EL-Refaie and T. M. Jahns, "Application of bi-state magnetic material to an automotive IPM starter/alternator machine," *IEEE Trans. Energy Convers.*, vol. 20, no. 1, pp. 71–79, Mar. 2005.
- [17] A. M. EL-Refaie, R. Manzke, and T. M. Jahns, "Application of bi-state magnetic material to automotive offset-coupled IPM starter/alternator machine," *IEEE Trans. Ind. Appl.*, vol. 40, no. 3, pp. 717–725, May/Jun. 2004.



**Ayman M. EL-Refaie** (S'95–M'05–SM'07–F'13) received the B.S. and M.S. degrees in electrical power engineering from Cairo University, Giza, Egypt, in 1995 and 1998, respectively, and the M.S. and Ph.D. degrees in electrical engineering from the University of Wisconsin–Madison, Madison, WI, USA, in 2002 and 2005, respectively.

Since 2005, he has been a Senior Engineer with the Electrical Machines Laboratory, GE Global Research Center, Niskayuna, NY, USA, where he has worked on several projects that involve the development of advanced electrical machines for various applications, including aerospace, traction, wind, and water desalination. He was the Program Manager and the Principal Investigator of a \$5.6 M Department of Energy (DOE)-funded project to develop next-generation traction motors for hybrid vehicles. He is currently the Program Manager and the Principal Investigator of a \$12 M DOE-funded project to develop next-generation traction motors for hybrid vehicles that do not include rare-earth materials. Between 1999 and 2005, he was a Research Assistant with the Wisconsin Electric Machines and Power Electronics Consortium Group, University of Wisconsin–Madison. Between 1995 and 1998, he was an Assistant Lecturer with Cairo University and The American University in Cairo. He has authored/coauthored 30 journal and 44 conference publications, with several others pending. He is a holder of 23 issued U.S. patents and has 28 U.S. patent applications, with several others pending. His interests include electrical machines and drives.

Dr. EL-Refaie is currently the Chair of the IEEE Industry Applications Society (IAS) Transportation Systems Committee and the General Chair for the IEEE Energy Conversion Conference and Exposition (ECCE) 2014. He was a Technical Program Chair for the IEEE ECCE 2011. He is an Associate Editor for the IAS Electric Machines Committee. He was a recipient of several management awards with GE, including the prestigious 2011 Albert W. Hull Award, the highest individual award for early career researchers. He was also the recipient of the "Forward under 40," which is awarded to outstanding University of Wisconsin alumni under the age of 40, from the Wisconsin Alumni Association in 2009 and the IEEE IAS "Andrew Smith Outstanding Young Member Award," also in 2009. He is a member of Sigma Xi.



**James P. Alexander** received the B.S.E.E. degree from the Polytechnic Institute of New York, Brooklyn, NY, USA, in 1983.

In 1985, he completed the Edison Engineering Development Program at the GE Global Research Center, Niskayuna, NY, where he is currently an Engineer in the Electrical Machines Laboratory. He completed graduate work at Rensselaer Polytechnic Institute, Troy, NY; the University of Wisconsin–Madison, Madison, WI, USA; and Purdue University, West Lafayette, IN, USA. He has 25 years of experience in the electrical and mechanical design of electrical machinery and nine years of experience with the design of magnetic resonance imaging magnets. He is a holder of 32 U.S. patents with several others pending.



**Steven Galioto** received the B.S. and M.E. degrees in electrical engineering from Rensselaer Polytechnic Institute, Troy, NY, USA, in 2003 and 2006, respectively.

He spent three years in the Edison Engineering Development Program at the GE Global Research Center, Niskayuna, NY, where he has been a Lead Engineer in the Electrical Machines Laboratory since 2006. He has coauthored several conference publications. He has several U.S. patent applications. His current technical focus areas include permanent-magnet machine design and analysis, as well as hybrid vehicle development for heavy-duty applications.



**Patel B. Reddy** (S'07–M'10) received the Bachelor's degree in electrical engineering from the Indian Institute of Technology Kharagpur, Kharagpur, India, in 2003, during which he worked in the area of stability of power electronic converters, and the Ph.D. degree in electrical and computer engineering from the University of Wisconsin–Madison, Madison, WI, USA, in 2010.

From 2004 to 2010, he was a Research Assistant with the Wisconsin Electric Machines and Power Electronics Consortium. Since 2010, he has been with the Electrical Machines Laboratory, GE Global Research Center, Niskayuna, NY, USA. His interests include electrical machines and drives.



**Kum-Kang Huh** (S'03–M'09) was born in Seoul, Korea. He received the B.S. and M.S. degrees in control and instrumentation engineering from Korea University, Seoul, Korea, in 1993 and 1995, respectively, and the Ph.D. degree in electrical engineering from the University of Wisconsin–Madison, Madison, WI, USA, in 2008.

Since 2008, he has been with the GE Global Research Center, Niskayuna, NY, USA, where he is currently an Electrical Engineer in the Electrical Machines Laboratory. Between 1995 and 2002, he was with the Mando Global R&D Center, Seoul, where he developed electric vehicle traction systems and electric power steering systems. His research interests include modeling, control, and diagnostics of electric machines and power electronics systems.



**Peter de Bock** received the M.S. degree from the University of Twente, Enschede, The Netherlands, in 2002 and the Ph.D. degree from the University of Cincinnati, Cincinnati, OH, USA, in 2013.

Since 2003, he has been a Senior Electronics Cooling Researcher with the GE Global Research Center, Niskayuna, NY, USA.

**Xiochun Shen** received the Ph.D. degree from the University of Michigan, Ann Arbor, MI, USA.

From April 2007 to May 2013, he was a Research Engineer with GE Global Research. Since May 2013, he has been a Manager–Engineering Analysis with Ensen plc.